BulkSpin-OrbitTorque-Driven Spin Hall Nano-OscillatorsUsing PtBi Alloys with Engineered Crystallinity

Citation for the original published paper (version of record):
Shashank, U., Kumar, A., Parvini, T. et al (2026). BulkSpin-OrbitTorque-Driven Spin Hall Nano-OscillatorsUsing PtBi Alloys with Engineered Crystallinity. ACS Applied Materials & Interfaces, 18(29): 39941-39951.
http://dx.doi.org/10.1021/acsami.6c06092

ACS APPLIED MATERIALS & INTERFACES

www.acsami.org

Research Article

Bulk Spin−Orbit Torque-Driven Spin Hall Nano-Oscillators Using PtBi Alloys with Engineered Crystallinity

Utkarsh Shashank, Akash Kumar, Tahereh Sadat Parvini, Hauke Heyen, Lunjie Zeng, Andrew B. Yankovich, Jong-Guk Choi, Mona Rajabali, Eva Olsson, Markus Münzenberg,* and Johan Åkerman*

Cite This: ACS Appl. Mater. Interfaces 2026, 18, 39941−39951

Read Online

ABSTRACT: Spin−orbit-torque-driven auto-oscillations in spin Hall nano-oscillators (SHNOs) provide a promising route toward energy-efficient, nanoscale microwave devices for neuromorphic computing and high-frequency technologies. Achieving robust oscillations requires lowering the threshold current (I_{th}), governed by the spin Hall efficiency (θ_{SH}). Conventional approaches to enhance θ_{SH} often involve trade-offs, such as increased resistivity and interfacial effects. Here, we demonstrate a pronounced enhancement of the bulk spin Hall effect in PtBi alloys via crystallographic engineering, achieving a 3-fold increase in θ_{SH} from 0.07 in $Pt_{100.0}Bi_{0.0}$ to 0.24 in $Pt_{94.0}Bi_{6.0}$ and 0.19 in $Pt_{91.3}Bi_{8.7}$, extracted from DC-bias spin-torque ferromagnetic resonance. The enhancement arises from bulk-dominated extrinsic side-jump scattering. Correspondingly, I_{th} is reduced by 42% and 32% in 100 nm SHNOs based on $Co_{40}Fe_{40}B_{20}$(3 nm)/$Pt_{94.0}Bi_{6.0}$(4 nm) and $Co_{40}Fe_{40}B_{20}$(3 nm)/$Pt_{91.3}Bi_{8.7}$(4 nm), respectively. The devices exhibit narrower linewidths (∼25 MHz), enhanced quality factors ($350 \leq Q \leq 550$, ∼4× higher than Pt ($Pt_{100.0}Bi_{0.0}$)), and a 61.6% reduction in threshold power. These findings establish PtBi alloys as efficient spin Hall materials, enabling reduced power consumption for SHNO-based neuromorphic and memory technologies.

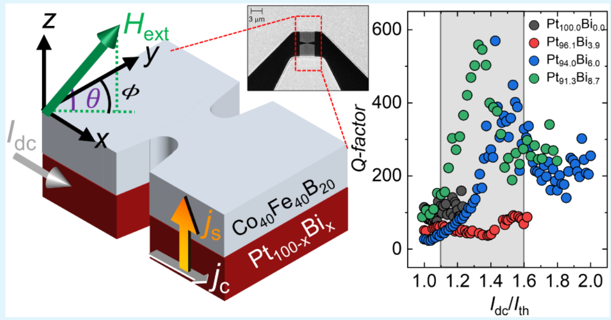

KEYWORDS: *spin−orbit torque, spin Hall effect, spin Hall nano-oscillator, auto-oscillation, extrinsic side-jump scattering*

■ INTRODUCTION

The efficient control of magnetization via spin−orbit torque (SOT),[1] primarily generated by the Spin Hall effect (SHE),[2,3] lies at the core of modern spintronics.[4] It plays a key role in magnetization switching,[5−8] in the generation and control of propagating spin waves,[9,10] in spin Hall nano-oscillators (SHNOs)[11,12] and in the movement of domain walls and skyrmions.[13−15] In a heavy metal (HM) with large spin−orbit coupling, the SHE generates a sizable transverse spin current density, $\mathbf{j}_s$, from a longitudinal charge current density, $\mathbf{j}_c$. The generated $\mathbf{j}_s$ can exert different torques on the magnetization of an adjacent ferromagnet (FM) layer, where the damping-like torque, $\boldsymbol{\tau}_{DL}$, is the component collinear with the intrinsic damping torque, $\boldsymbol{\tau}_\alpha$, of the FM layer.[16] If $\boldsymbol{\tau}_{DL}$ balances $\boldsymbol{\tau}_\alpha$, the threshold condition for FM auto-oscillations (AO), with a corresponding threshold current (I_{th}), is reached in the SHNO.[17,18] Over the past decade, SOT-driven nanoconstriction-based SHNOs have garnered significant attention thanks to their straightforward nanofabrication, direct optical and gate access to the auto-oscillating FM region, and rich magnetodynamical behavior.[19] SHNOs have shown tremendous promise for mutual synchronization in chains[20,21] and arrays,[22−24] paving the way for applications in neuromorphic computing,[25−27] Ising machines,[28] magnonic conduits,[10] and high-frequency GHz technologies.[29]

To reduce I_{th}, a higher conversion of $\mathbf{j}_c$ to $\mathbf{j}_s$, defined as the spin Hall efficiency, θ_{SH}, is required. θ_{SH} can be expressed as $\mathbf{j}_s = \frac{\hbar}{2e}\theta_{SH}(\mathbf{j}_c \times \hat{\boldsymbol{\sigma}})$, where $\hat{\boldsymbol{\sigma}}$ is the polarization of the spin current, e is the elementary charge, and $\hbar$ is the reduced Planck constant. The most commonly used HM, Pt, has a moderate $\theta_{SH} \approx 0.05−0.09$, arising from its intrinsic SHE.[16,30−32] Ion implantation[33−36] or sputtering[37−39] of nonmetallic, lighter impurities, such as S, O, N, and P, can also be used to tune the θ_{SH} of Pt, Ta, and W. However, such tuning requires careful materials engineering and often comes with a trade-off in the form of increased longitudinal resistivity (ρ_{xx}), as observed in TaN, which can exhibit values as high as 3000 $\mu\Omega$·cm.[39] In contrast, metallic impurities introduced by cosputtering with

Received: March 26, 2026
Revised: June 19, 2026
Accepted: June 24, 2026
Published: July 13, 2026

https://doi.org/10.1021/acsami.6c06092
ACS Appl. Mater. Interfaces 2026, 18, 39941−39951

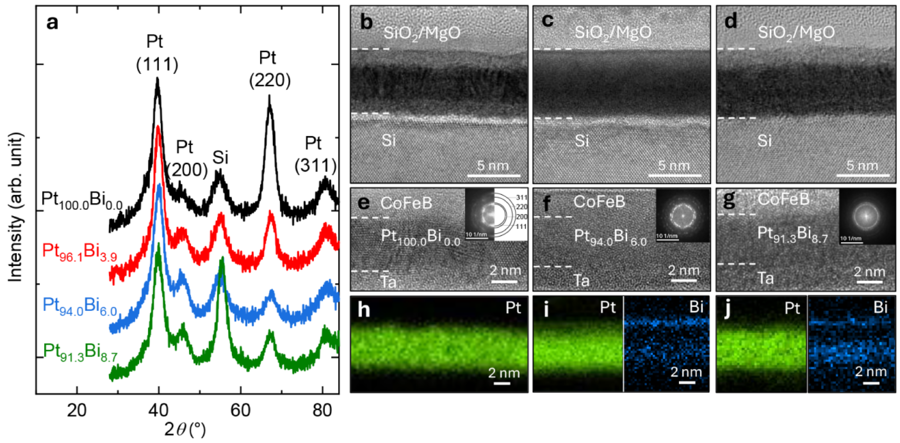

Figure 1. (a) GIXRD patterns of the $Pt_{100.0}Bi_{0.0}$ stack (black) and PtBi alloy stacks with compositions $Pt_{96.1}Bi_{3.9}$ (red), $Pt_{94.0}Bi_{6.0}$ (blue), and $Pt_{91.3}Bi_{8.7}$ (green). (b−d) Cross-sectional TEM images of (b) the $Pt_{100.0}Bi_{0.0}$ stack (HR-Si/Ta(2.4 nm)/Pt(4.0 nm)/$Co_{40}Fe_{40}B_{20}$(3.0 nm)/MgO(2.0 nm)/SiO_2(3.0 nm)), (c) the $Pt_{94.0}Bi_{6.0}$ stack (HR-Si/Ta(2.4 nm)/$Pt_{94.0}Bi_{6.0}$(4.0 nm)/$Co_{40}Fe_{40}B_{20}$(3.0 nm)/MgO(2.0 nm)/SiO_2(3.0 nm)), and (d) the $Pt_{91.3}Bi_{8.7}$ stack (HR-Si/Ta(2.4 nm)/$Pt_{91.3}Bi_{8.7}$(4.0 nm)/$Co_{40}Fe_{40}B_{20}$(3.0 nm)/MgO(2.0 nm)/SiO_2(3.0 nm)), all showing uniform, well-defined layers with comparable total thicknesses. (e−g) High-resolution TEM images of the same stacks with diffractograms obtained from HR-TEM images in respective insets. (e) The $Pt_{100.0}Bi_{0.0}$ stack shows clear lattice fringes and sharp Bragg spots (inset diffractogram), indicative of a crystalline Pt structure. The distinct and indexed (220) and (111) spots confirm the crystalline face-centered cubic (fcc) nature of the $Pt_{100.0}Bi_{0.0}$ layer. (f, g) The $Pt_{94.0}Bi_{6.0}$ and $Pt_{91.3}Bi_{8.7}$ stacks display more disordered lattice fringes and reduced intensity of higher order (220 and 311) diffraction rings in the diffractograms (insets), suggesting lower crystallinity. (h−j) STEM-EDXS elemental maps of Pt and Bi for the $Pt_{100.0}Bi_{0.0}$, $Pt_{94.0}Bi_{6.0}$, and $Pt_{91.3}Bi_{8.7}$ stacks, respectively. Bi is uniformly distributed within the $Pt_{94.0}Bi_{6.0}$ and $Pt_{91.3}Bi_{8.7}$ layers, with enrichment at the PtBi/$Co_{40}Fe_{40}B_{20}$ interface. Additional HAADF-STEM images and STEM-EDXS elemental maps and line profiles are provided in Figures S1 and S2.

the HM neither require complex engineering nor introduce drastic changes in ρ_{xx}. A better trade-off between θ_{SH} and ρ_{xx} is crucial for low-power consumption in SOT magnetic random-access memory (SOT-MRAM).[36,40] In this context, Pt-, Ta-, and W-based alloys have been explored (θ_{SH} values in parentheses), such as $Pt_{28}Cu_{72}$ (0.07),[41] $Pt_{75}Pd_{25}$ (0.26),[42] $Pt_{90}Pd_{10}$ (0.17),[43] $Pt_{92}Bi_8$ (0.10),[44] $Pt_{88}Mo_{12}$ (0.35),[45] $Pt_{70}Gd_{30}$ (0.27),[46] $Pt_{75}Au_{25}$ (0.35),[47] $Pt_{53}Au_{47}$ (0.32);[48] $W_{100-x}Ta_x$ (−0.35 to −0.62),[49] and $Cu_{100-x}Ta_x$ (−0.04 to −0.09).[39] Within this framework, Hayashi et al. showed that $Pt_{100-x}Bi_x$/Co bilayers with substantial Bi concentrations (x = 25−50) exhibit markedly improved θ_{SH} and reduced switching current densities relative to Pt, identifying PtBi as a strong candidate for energy-efficient magnetization switching.[50] Complementing this, Münzenberg et al. demonstrated that $Pt_{92}Bi_8$-based heterostructures can act as high-performance THz spintronic emitters, delivering broader bandwidths and higher central frequencies than conventional bilayer systems.[51] In addition, at higher Bi concentrations, such as in stoichiometric $PtBi_2$, this material has attracted attention as a topological system, exhibiting giant three-dimensional Rashba-like spin splitting ($\alpha_R \approx 4.36$ eV·Å)[52] and surface-bound superconducting gaps reaching up to 20 meV.[53] However, when the Bi content exceeds $x \geq 60\%$, $Pt_{100-x}Bi_x$ alloys transition toward the $PtBi_2$ phase,[50] leading to degraded spin Hall conductivity (σ_{SH}^{xy}) due to increased ρ_{xx}, which causes significant current shunting into the FM layer, resulting in Joule heating and deterioration of spectral quality in SHNOs, as illustrated in our previous work.[22] Therefore, optimization at moderate Bi levels is paramount for attaining practical device applications, especially SHNOs. Furthermore, despite these advances, a unified understanding of the reciprocal connection between θ_{SH} and I_{th} in $Pt_{100-x}Bi_x$ alloys via both ST-FMR and direct AO measurements remains unexplored.

Here, we report on a dramatic increase in θ_{SH} by more than three times when alloying Pt with Bi, and a corresponding decrease of I_{th} by 42% in SHNOs based on $Pt_{94.0}Bi_{6.0}$ and $Co_{40}Fe_{40}B_{20}$. We deposited $Pt_{100-x}Bi_x$ alloy thin films using electron-beam coevaporation and systematically varied the Bi concentrations across x = 0.0, 3.9, 6.0, and 8.7 (hereafter denoted as $Pt_{100.0}Bi_{0.0}$, $Pt_{96.1}Bi_{3.9}$, $Pt_{94.0}Bi_{6.0}$, and $Pt_{91.3}Bi_{8.7}$, respectively). Structural characterization by grazing-incidence X-ray diffraction (GIXRD) and transmission electron microscopy (TEM) reveals a progressive loss of crystallinity with increasing Bi content, suggesting enhanced scattering contributions via crystallographic engineering. Scanning transmission electron microscopy (STEM) and energy-dispersive X-ray spectroscopy (EDXS) investigation indicates a uniform distribution of Bi in Pt. Linewidth analysis of DC-biased spin-torque ferromagnetic resonance (ST-FMR) measurements vs current yields a sharp increase in θ_{SH} from 0.07 ± 0.01 in $Pt_{100.0}Bi_{0.0}$ to 0.24 ± 0.02 and 0.19 ± 0.01 in the $Pt_{94.0}Bi_{6.0}$ and $Pt_{91.3}Bi_{8.7}$ alloys, respectively. To rule out artifacts and confirm the bulk origin of SOT, we demonstrate a clear sin 2ϕ cos ϕ in-plane angular dependence of the SOT for all PtBi alloys. Thanks to the increase in θ_{SH}, we observe a 42% and 32% reduction in I_{th} for $Pt_{94.0}Bi_{6.0}$ and $Pt_{91.3}Bi_{8.7}$-based 100 nm SHNOs. These PtBi-based SHNOs further exhibit narrower linewidth (Δf) (≈ 25 MHz), enhanced quality factors of ≈350 ≤ Q ≤ 550, about ∼4× higher than $Pt_{100.0}Bi_{0.0}$, and lower normalized input power (61.6% reduction). Our findings of a higher θ_{SH} driven by bulk-extrinsic SHE, accompanied by a reduced I_{th}, establish Bi alloying in Pt as a robust strategy for engineering energy-efficient SHNOs, opening new avenues beyond conventional 5d transition metals.

https://doi.org/10.1021/acsami.6c06092
ACS Appl. Mater. Interfaces 2026, 18, 39941−39951

■ RESULTS AND DISCUSSION

Structural Characterization via GIXRD and TEM

Figure 1a shows out-of-plane grazing-incidence X-ray diffraction (GIXRD) patterns of $Pt_{100-x}Bi_x$ thin films (see Experimental Section). Reflections from the (111), (200), (220), and (311) planes confirm a crystalline face-centered cubic (*fcc*) phase in $Pt_{100.0}Bi_{0.0}$ and $Pt_{96.1}Bi_{3.9}$.[36,54] Increasing the Bi content reduces the overall reflection intensities, particularly that of the (220) peak, indicating a reduction in crystallinity.[36,55] Peak broadening becomes more pronounced in $Pt_{94.0}Bi_{6.0}$ and $Pt_{91.3}Bi_{8.7}$. The intensity ratio $I_{(111)}/I_{(220)}$ rises from 0.385 (0% Bi) to 1.645 (6% Bi), then falls to 1.070 at 8.7% Bi. Similarly, the out-of-plane lattice parameter increases from 3.9525 to 3.9653 Å (0−6% Bi), followed by a slight decrease to 3.9595 Å at 8.7% Bi. This nonmonotonic trend suggests a shift in preferred crystallographic orientation, likely due to strain-induced texturing at higher Bi concentrations, consistent with previous reports.[50] The extracted out-of-plane lattice parameters and texture-related peak intensity ratios are summarized in Table 1.

Table 1. Extracted Out-of-Plane Lattice Parameters and Relative Peak Intensity Ratios Obtained from GIXRD Measurements of $Pt_{100-x}Bi_x$ Films[a]

Composition	I(111)/I(220)	Lattice parameter, *a* (Å)
$Pt_{100.0}Bi_{0.0}$	0.385	3.9525
$Pt_{96.1}Bi_{3.9}$	0.852	3.9558
$Pt_{94.0}Bi_{6.0}$	1.645	3.9653
$Pt_{91.3}Bi_{8.7}$	1.070	3.9595

[a]The variation in the I(111)/I(220) ratio indicates changes in crystallographic texture with increasing Bi concentration.

Figure 1b−d displays cross-sectional TEM images of the $Pt_{100.0}Bi_{0.0}$ stack, the $Pt_{94.0}Bi_{6.0}$ stack, and the $Pt_{91.3}Bi_{8.7}$ stack, respectively. All stacks exhibit well-defined, uniform layered structures with comparable total thicknesses. Figure 1e−g presents HRTEM images of the samples. In the $Pt_{100.0}Bi_{0.0}$ (Figure 1e), clear lattice fringes are visible, and the diffractogram (inset) shows distinct Bragg spots and rings, indicating a crystalline structure of the Pt layer.[33,36] In contrast, the $Pt_{94.0}Bi_{6.0}$ sample (Figure 1f) exhibits more disordered lattice fringes and diminished Bragg spots and higher-order (220 and 311) rings (inset diffractogram), suggesting reduced crystallinity, consistent with the GIXRD results. Furthermore, for the $Pt_{91.3}Bi_{8.7}$ sample (Figure 1g), the lattice fringes become faintest, and the Bragg spots are further diminished, indicating an even greater reduction in crystallinity.[36] Figure 1h−j provides STEM-EDXS elemental maps for the same samples. In both the $Pt_{94.0}Bi_{6.0}$ and $Pt_{91.3}Bi_{8.7}$ stacks, Bi is uniformly distributed throughout the target Pt layer, with no sign of clustering. An enrichment of Bi is also observed at the $Pt_{94.0}Bi_{6.0}/Co_{40}Fe_{40}B_{20}$ and $Pt_{91.3}Bi_{8.7}/Co_{40}Fe_{40}B_{20}$ interfaces. The impact of both bulk and interfacial Bi distributions on the SHE in Pt is addressed in subsequent sections.

Spin-Torque Ferromagnetic Resonance Measurements

To evaluate how Bi doping modulates the SHE in Pt, we performed spin-torque ferromagnetic resonance (ST-FMR) measurements[16] (see Experimental Section for details). Figure 2a illustrates the schematic of the ST-FMR measurement and Figure 2b shows the experimental setup. An in-plane microwave current I_{rf} with a power of 4 dBm was applied along the *x*-axis of the HM/FM bilayer via a ground-source-ground (GSG) coplanar waveguide (CPW). The external in-plane magnetic field H_{ext} was swept ± 500 mT at an angle ϕ = 70° between I_{rf} and H_{ext}. The charge current density $\mathbf{j}_c$ (along *x*) driven by I_{rf} generates a spin current density $\mathbf{j}_s$ along *z* with

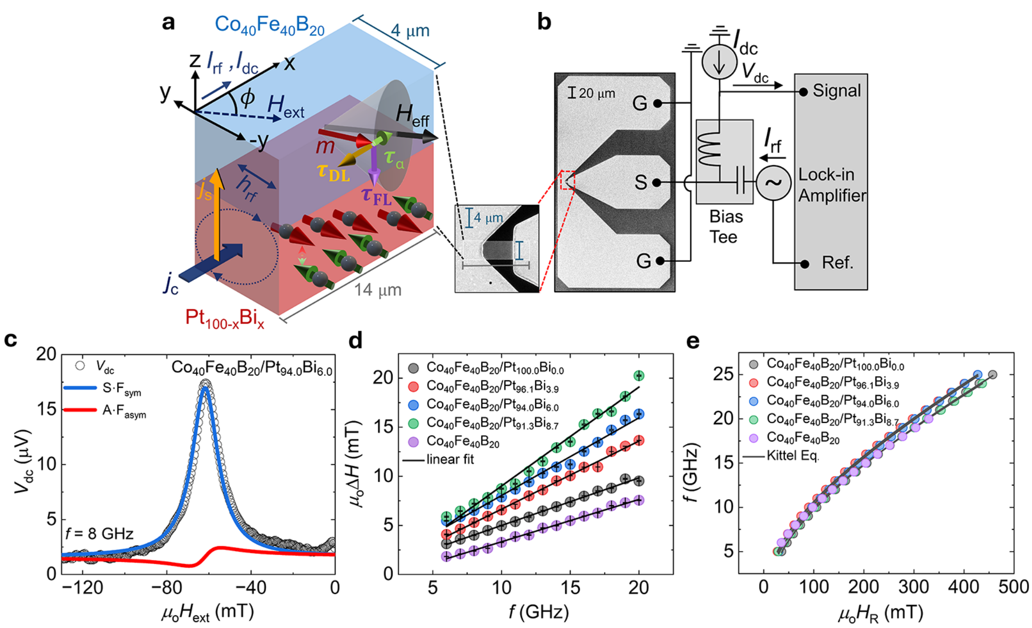

Figure 2. (a) Schematic of the SHE and the microscopic mechanism of the ST-FMR excitation, depicting the torques acting on the FM magnetization. (b) The ST-FMR measurement technique and detection principle along with the microbar device connected to a GSG-CPW. A zoom-in SEM image of the red square shows the microbar. (c) ST-FMR voltage (V_{dc}) at f = 8 GHz of $Pt_{94.0}Bi_{6.0}$, with separate symmetric and antisymmetric components fit to eq 1. (d) ΔH vs f and (e) f vs H_R for f = 6−20 GHz, with solid black lines being linear fits to eq 2 for all samples evaluated in this study, including $Co_{40}Fe_{40}B_{20}$. Solid lines in (e) represent fits to the Kittel eq 3.

https://doi.org/10.1021/acsami.6c06092
ACS Appl. Mater. Interfaces 2026, 18, 39941−39951

Table 2. Extracted Magnetic and Linewidth Fitting Parameters Obtained from ST-FMR Measurements[a]

Stack	α_{total}	ΔH_0 (mT)	$\mu_0 M_{eff}$ (mT)	$\mu_0 H_k$ (mT)
$Co_{40}Fe_{40}B_{20}/Pt_{100.0}Bi_{0.0}$	0.0140 ± 0.0005	0.2877 ± 0.2530	1141.38 ± 4.36	12.17
$Co_{40}Fe_{40}B_{20}/Pt_{96.1}Bi_{3.9}$	0.0200 ± 0.0007	0.5675 ± 0.3465	1268.79 ± 0.83	5.12
$Co_{40}Fe_{40}B_{20}/Pt_{94.0}Bi_{6.0}$	0.0230 ± 0.0010	0.2690 ± 0.6140	1268.43 ± 7.22	9.95
$Co_{40}Fe_{40}B_{20}/Pt_{91.3}Bi_{8.7}$	0.0290 ± 0.0020	0.1054 ± 0.9418	1088.84 ± 3.48	4.69
$Co_{40}Fe_{40}B_{20}$	0.0120 ± 0.0004	0.1760 ± 0.2260	1038.91 ± 1.51	2.75

[a]Here, ΔH_0 represents the inhomogeneous linewidth broadening obtained from the linear fit intercept in Figure 2d.

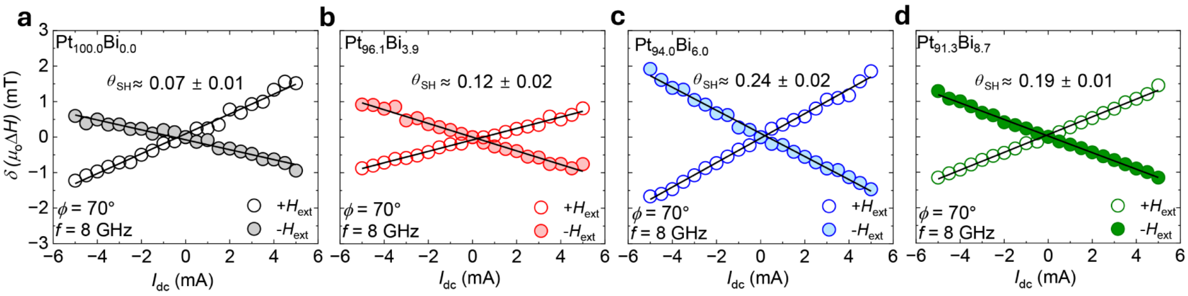

Figure 3. Current-induced modulation of linewidth, $\delta(\mu_0\Delta H)$ as a function of I_{dc} at $f = 8$ GHz for (a) $Pt_{100.0}Bi_{0.0}$, (b) $Pt_{96.1}Bi_{3.9}$, (c) $Pt_{94.0}Bi_{6.0}$, and (d) $Pt_{91.3}Bi_{8.7}$. Open circles correspond to positive magnetic field sweep ($+H_{ext}$), while filled circles correspond to negative sweep ($-H_{ext}$). The solid black lines are linear fits. The increasing slope of $\delta(\mu_0\Delta H)/I_{dc}$ with Bi impurity in Pt indicates enhanced θ_{SH}.

spin polarization $\hat{\boldsymbol{\sigma}}$ along $-y$. This $\mathbf{j}_s$ exerts an in-plane $\boldsymbol{\tau}_{DL}$ on the magnetization $\mathbf{m}$ of the FM layer. Simultaneously, the Oersted field, h_{rf}, generated by I_{rf} acts as an out-of-plane Oersted field torque, $\boldsymbol{\tau}_{OF}$. Interfacial effects, rather than bulk mechanisms, can also induce out-of-plane field-like torques ($\boldsymbol{\tau}_{FL}$) arising from the Rashba effect, particularly in thinner FM layers ($\lesssim$1 nm) interfaced with HM,[56] which may overlap with $\boldsymbol{\tau}_{OF}$. When $\boldsymbol{\tau}_{FL}$ is small, as in bulk SHE heterostructures, the combined torques ($\boldsymbol{\tau}_{DL}$ and $\boldsymbol{\tau}_{OF}$) govern the magnetization precession. The precession of $\mathbf{m}$ around the effective field H_{eff} induces a time-dependent resistance variation via the anisotropic magnetoresistance (AMR), $\Delta R \propto \cos^2 \phi$ (see Figure S3). Mixing with I_{rf}, the varying ΔR generates a rectified ST-FMR voltage, V_{dc}. The I_{rf} was amplitude modulated at 98.76 Hz, serving as a reference signal for lock-in detection.

Figure 2c shows the ST-FMR voltage spectrum measured at frequency $f = 8$ GHz and $I_{dc} = 0$ mA for $Pt_{94.0}Bi_{6.0}$. The measured V_{dc} is defined as[16]

$$V_{dc} = SF_{sym}(H_{ext}) + AF_{asym}(H_{ext}) \quad (1)$$

where $F_{sym}(H_{ext}) = \frac{(\Delta H)^2}{(\mu_0 H_{ext} - \mu_0 H_R)^2 + (\Delta H)^2}$ is the symmetric component, and $F_{asym}(H_{ext}) = \frac{\Delta H(\mu_0 H_{ext} - \mu_0 H_R)}{(\mu_0 H_{ext} - \mu_0 H_R)^2 + (\Delta H)^2}$ is the antisymmetric component. The parameters S and A are the weight factors corresponding to the symmetric and antisymmetric components, respectively. ΔH and H_R are the linewidth (half-width-at-half-maximum) and resonance field of the ST-FMR spectra, respectively. Strikingly, a very high symmetric component $SF_{sym}(H_{ext})$, confirming the high $\boldsymbol{\tau}_{DL}$, is observed for $Pt_{94.0}Bi_{6.0}$. Furthermore, in-plane angular ST-FMR measurements reveal that both the S and A weight factors exhibit a clear $\sin 2\phi \cos \phi$ dependence across all $Pt_{100-x}Bi_x$ compositions (see Figure S4 for details). This angular dependence is characteristic of a conventional bulk-SOT origin, free from torque symmetry breaking, and rules out significant contributions from experimental artifacts.[36,57−60]

Next, we extract the Gilbert damping parameter α_{total} by plotting ΔH as a function of f (see Figure 2d), using the relation

$$\Delta H = \Delta H_0 + \frac{2\pi\alpha_{total}}{\gamma\mu_0} f \quad (2)$$

where ΔH_0 denotes the frequency-independent inhomogeneous linewidth broadening,[61] and γ is the gyromagnetic ratio. A systematic increase in α_{total} is observed from 0.0120 ± 0.0004 ($Co_{40}Fe_{40}B_{20}$) to 0.0140 ± 0.0005 ($Co_{40}Fe_{40}B_{20}/Pt_{100.0}Bi_{0.0}$) to 0.0200 ± 0.0007, 0.0230 ± 0.0010, and 0.0290 ± 0.0020 for $Co_{40}Fe_{40}B_{20}/Pt_{96.1}Bi_{3.9}$, $Co_{40}Fe_{40}B_{20}/Pt_{94.0}Bi_{6.0}$, and $Co_{40}Fe_{40}B_{20}/Pt_{91.3}Bi_{8.7}$, respectively. This trend reflects enhanced spin current generation, potentially arising from spin pumping[44] and/or an increase in SHE.[34,35] The extracted ΔH_0 remains low and positive (0.1054−0.5675 mT, see Table 2), indicating excellent film quality.[33,34] Figure 2e depicts the frequency dependence of the resonance field, H_R, using the Kittel formula:

$$f = \frac{\gamma\mu_0}{2\pi}\sqrt{(H_R + H_K)(H_R + H_K + M_{eff})} \quad (3)$$

where H_K is the in-plane magnetic anisotropy field and M_{eff} is the effective demagnetization.[62] The extracted $\mu_0 M_{eff}$ values, 1038.91 mT ($Co_{40}Fe_{40}B_{20}$ without Pt or PtBi layer), 1141.38 mT ($Pt_{100.0}Bi_{0.0}$), 1268.79 mT ($Pt_{96.1}Bi_{3.9}$), 1268.43 mT ($Pt_{94.0}Bi_{6.0}$), and 1088.84 mT ($Pt_{91.3}Bi_{8.7}$), along with H_K values of 2.75−12.17 mT, confirm no significant variation in magnetic properties upon Bi incorporation. The extracted magnetic and linewidth fitting parameters are summarized in Table 2.

To quantify θ_{SH}, we use DC-bias ST-FMR,[16] where a direct current I_{dc} is applied simultaneously with I_{rf} under an external in-plane magnetic field H_{ext} to modulate the linewidth ΔH. Figure 3a−d shows the change in linewidth, $\delta(\mu_0\Delta H)$, as a function of I_{dc} at $f = 8$ GHz, measured at an angle $\phi = 70°$ with an input power of 4 dBm. Here, ϕ is the angle between the combined current direction ($I_{rf} + I_{dc}$) and the external field

https://doi.org/10.1021/acsami.6c06092
ACS Appl. Mater. Interfaces 2026, 18, 39941−39951

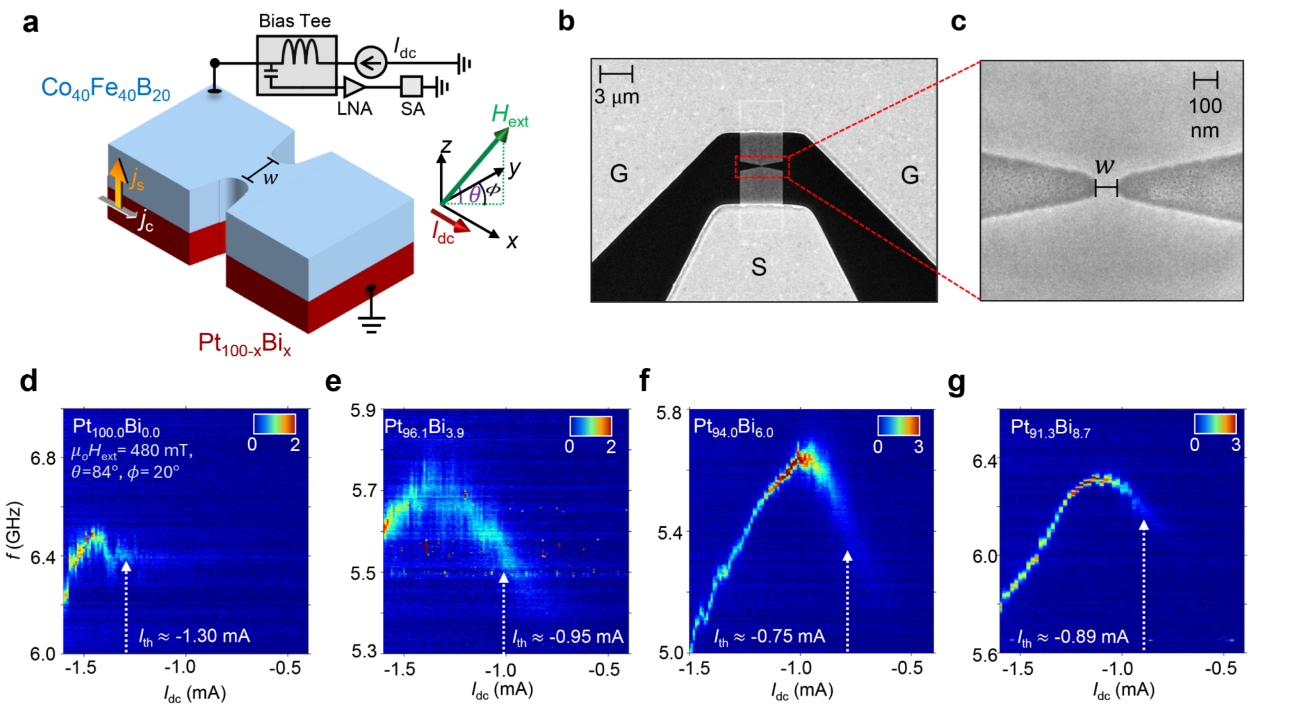

Figure 4. (a) Schematic of the SHNO and measurement setup. (b) SEM image of the GSG-based CPW with SHNO. (c) Enlarged SEM of the 100 nm wide SHNO (black scale bars in b, c). PSD from the 100 nm SHNO as a function of I_{dc} at μ_0H_{ext} = 480 mT, ϕ = 20°, θ = 84° for (d) $Pt_{100.0}Bi_{0.0}$, (e) $Pt_{96.1}Bi_{3.9}$, (f) $Pt_{94.0}Bi_{6.0}$, and (g) $Pt_{91.3}Bi_{8.7}$. Color bars indicate peak power (dB above noise floor). The white arrows mark the respective I_{th}.

H_{ext}. The angle ϕ = 70° was chosen to maximize the linewidth modulation since sin ϕ reaches near its peak between 70° and 75°, and the AMR also exhibits significant variation within the 45°−75° range[18,63] fruitful for a clean ST-FMR spectrum. The change in linewidth is defined as $\delta(\mu_0\Delta H) = \mu_0\Delta H|_{I_{dc}} - \mu_0\Delta H|_{I_{dc}=0}$, which varies linearly with I_{dc}. Reversing the polarity of H_{ext} from positive H_{ext} at ϕ = 70° to negative H_{ext} at ϕ = 250° reverses the magnetization direction of $Co_{40}Fe_{40}B_{20}$, which correspondingly reverses the slope of $\delta(\mu_0\Delta H)/I_{dc}$, consistent with the conventional SHE-driven SOT mechanism.[36] Using a parallel-resistor model (see Section S5 for details on calculating ρ_{xx}) and Figure S5 for ρ_{xx} values, we estimate the current density in the HM layer, $j_{dc,HM}$, and extract θ_{SH} from the slope $\frac{\Delta[\delta(\mu_0\Delta H)]}{\Delta j_{dc,HM}}$ according to[16]

$$\theta_{SH} = \frac{2e}{\hbar}\frac{\left(H_R + \frac{M_{eff}}{2}\right)\mu_0 M_s t}{\sin\phi}\frac{\gamma}{2\pi f}\left|\frac{\Delta[\delta(\mu_0\Delta H)]}{\Delta j_{dc,HM}}\right| \tag{4}$$

where M_s and t are the saturation magnetization and thickness of $Co_{40}Fe_{40}B_{20}$, respectively, and M_{eff} is the effective demagnetization obtained from Kittel fitting.[61,64] We observe a slight increase in θ_{SH} from 0.07 ± 0.01 ($Pt_{100.0}Bi_{0.0}$) to 0.12 ± 0.02 ($Pt_{96.1}Bi_{3.9}$), with a small doping of 3.9%. However, increasing the Bi concentration to 6.0% and 8.7% yields a remarkable enhancement in θ_{SH} to 0.24 ± 0.02 ($Pt_{94.0}Bi_{6.0}$) and 0.19 ± 0.01 ($Pt_{91.3}Bi_{8.7}$). In particular, the highest θ_{SH} occurs at higher Bi concentrations where Pt loses its crystalline texture, as seen in Figure 1. This supports the correlation between reduced crystallinity and enhanced θ_{SH} in 5*d* transition metals. Recent experimental studies by Parkin et al.[40] and Shashank et al.[36] have similarly demonstrated that θ_{SH} peaks near the crystalline−amorphous boundary, where extrinsic scattering from impurities is maximized.

Spin Hall Nano-Oscillators

We fabricated 100 nm wide SHNOs and measured AO on all $Co_{40}Fe_{40}B_{20}/Pt_{100-x}Bi_x$ heterostructures to observe the effect of a higher θ_{SH} on I_{th}. See Experimental Section for details. A schematic of the setup is shown in Figure 4a. A direct current, I_{dc} (along the *x*-axis), was applied through a bias tee, while the resulting microwave signals were extracted through the high-frequency port, amplified using a low-noise amplifier (LNA), and analyzed with a spectrum analyzer (SA). A moderate out-of-plane field (θ = 84°) was selected to achieve a weak negative nonlinearity.[65] The in-plane angle, ϕ = 20°, was chosen to ensure adequate electrical sensitivity of the signal (ϕ is the angle between the *y*-axis and H_{ext}).

Figure 4b shows the scanning electron microscope (SEM) image of the device under test, and Figure 4c presents the enlarged SEM image of the 100 nm wide SHNO. The actual measured width *w* is in good agreement with the nominal design value. To understand the reciprocal relationship between the enhancement in θ_{SH} and the reduction in I_{th}, we performed current-dependent AO and extracted the power spectral density (PSD) generated by the 100 nm wide SHNO under μ_0H_{ext} = 480 mT (ϕ = 20° and θ = 84°) for all samples, as shown in Figure 4d−g. A nonmonotonic current dependence of the AO frequency is observed, attributed to a localized AO bullet mode promoted by negative nonlinearity, $\mathcal{N}$, typical for a FM layer with its magnetization far from the film normal.[65] The I_{th} is −1.30 mA for $Pt_{100.0}Bi_{0.0}$, decreasing to −0.95 mA for $Pt_{96.1}Bi_{3.9}$. At higher Bi concentrations, I_{th} drops significantly to −0.75 mA (42% reduction) for $Pt_{94.0}Bi_{6.0}$ and −0.89 mA (32% reduction) for $Pt_{91.3}Bi_{8.7}$. Concurrently, the PSD maps in Figure 4d−g show that $Pt_{94.0}Bi_{6.0}$ and $Pt_{91.3}Bi_{8.7}$ reach peak powers of ∼3 dB above the noise floor, clearly

https://doi.org/10.1021/acsami.6c06092
ACS Appl. Mater. Interfaces 2026, 18, 39941−39951

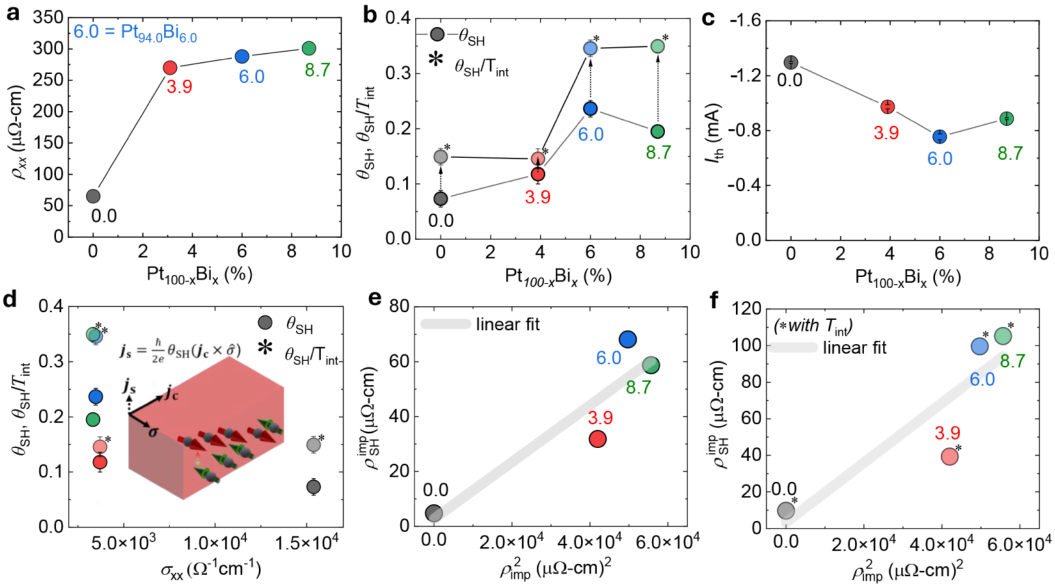

Figure 5. (a, b) Electrical resistivity, ρ_{xx}, θ_{SH} (solid circles), and interface-corrected θ_{SH}/T_{int} (translucent circles) versus Bi content x in $Pt_{100-x}Bi_x$ (at.%). (c) I_{th} versus Bi content. (d) θ_{SH} and θ_{SH}/T_{int} plotted against σ_{xx}; inset shows schematic of bulk spin Hall effect in PtBi alloy. (e) Impurity-induced spin Hall resistivity ρ_{imp}^{SH} versus impurity resistivity squared ρ_{imp}^2 (without transparency correction). (f) Same plot as (e) but corrected using T_{int}, showing that the linear scaling $\rho_{imp}^{SH} \propto \rho_{imp}^2$ persists. Error bars in (b, d) represent the standard error from eqs 2 and 4; in (c), mean deviation (MD) from I_{th} data sets (see Figure S7 and Experimental Section for details).

exceeding the ∼2 dB observed for $Pt_{100.0}Bi_{0.0}$ and $Pt_{96.1}Bi_{3.9}$. The integrated spectral power is likewise enhanced, while the linewidth is reduced, indicating stronger and more coherent auto-oscillations at higher Bi concentrations, which is advantageous for wireless communication applications.[24] Additional auto-oscillation measurements performed at $\mu_0 H_{ext}$ = 520−680 mT (see Figure S7) show that the extracted I_{th} exhibits only weak dependence on the applied magnetic field within this highly out-of-plane field geometry, consistent with previous reports on nanoconstriction SHNOs where the threshold current is governed by the interplay between the Gilbert damping parameter α_{total}, internal field, spin-wave localization, and spin−orbit torque.[66] See Figure S6 for AMR, Figure S7 for AO at other fields, Figure S8 for I_{th} extraction, and Figure S9 for peak power, output power, and linewidth.

Reciprocity, Interfacial Transparency, and Mechanism of Spin Hall Effect in PtBi Alloys

Building on the structural analysis and the observed reciprocity between ST-FMR and AO, several key parameters, ρ_{xx}, T_{int}, θ_{SH} (including T_{int}), and I_{th}, are analyzed across all $Pt_{100-x}Bi_x$ alloys (see Figures 5a−c, S9 and S10). The electrical resistivity ρ_{xx} increases with Bi concentration, rising from 65 $\mu\Omega$·cm for 0.0% Bi to 270, 288, and 301 $\mu\Omega$·cm for 3.9%, 6.0%, and 8.7% Bi, respectively (Figure 5a). To account for interfacial transparency effects, we evaluated the interfacial spin transparency T_{int} following the standard method by Parkin et al.[32] T_{int} was determined using the effective spin mixing conductance[35] $g_{eff}^{\uparrow\downarrow}$ obtained from linewidth broadening, the real part of the spin mixing conductance $G^{\uparrow\downarrow}$, and the spin diffusion length $\lambda_{sd} \propto 1/\rho_{xx}$ (Elliott−Yafet mechanism). The resulting T_{int} values gradually increase with Bi concentration, reflecting improved spin-current transmission across the $Co_{40}Fe_{40}B_{20}/Pt_{100-x}Bi_x$ interface (see Figure S10). When normalizing θ_{SH} by T_{int}, the overall trend remains unchanged: θ_{SH}/T_{int} increases up to 6% Bi and saturates beyond this concentration, confirming that the primary enhancement originates from bulk PtBi alloying rather than interface effects. The reported θ_{SH} values in the main text thus represent lower bounds, while θ_{SH}/T_{int} provides an interface-corrected estimate (see Figure 5b). For 0.0% and 3.9% Bi doping, θ_{SH} increases from 0.07 to 0.12, with a corresponding rise in ρ_{xx} from 65 to 270 $\mu\Omega$·cm, reducing I_{th} from −1.30 mA to −0.97 mA. At 6.0% Bi, ρ_{xx} rises marginally to 288 $\mu\Omega$·cm, while θ_{SH} significantly rises to 0.24 (3.4× increase), yielding the lowest I_{th} of −0.75 mA (42% reduction). At 8.7% Bi, ρ_{xx} further increases to 301 $\mu\Omega$·cm, but θ_{SH} decreases slightly to 0.19, still 2.7× higher than 0.0% Bi ($Pt_{100.0}Bi_{0.0}$), causing I_{th} to slightly rise to −0.89 mA, but still 32% lower than 0.0% Bi. Importantly, the 3.4× and 2.7× enhancement in θ_{SH} directly corresponds to the 42% and 32% reduction in I_{th}, respectively, establishing a clear correlation between θ_{SH} enhancement and I_{th} suppression, as shown in Figure 5b,c. This correspondence strengthens the conclusion that 6−8.7% Bi marks the critical range governing both microstructural evolution and spin transport behavior in PtBi alloys. Notably, the spin pumping study[44] also reports that θ_{SH} peaks within the 6−8% Bi range, consistent with the critical compositional window identified in our work. Despite the increase in α_{total} with Bi doping, the enhanced $\boldsymbol{\tau}_{DL}$ from the SHE compensates for $\boldsymbol{\tau}_{\alpha}$, leading to a reduction in I_{th}. This reduction would likely have been more significant if α_{total} had remained constant or decreased, complicating the direct assessment of SOT effects. The actual effect of torque on the AO is thus likely underestimated, and FM layers with lower α_{total}, such as GdFeCo,[61] could further enhance the reduction in I_{th}. Furthermore, this interplay between θ_{SH} and ρ_{xx} is critical for minimizing power consumption, expressed by the factor ρ_{xx}/θ_{SH}^2 relevant for SOT-MRAM applications, which improves at higher Bi concentrations (6.0% and 8.7%).[36,40]

To elucidate the mechanism underlying the SHE, we examine electrical conductivity σ_{xx}. Figure 5d shows θ_{SH} and

https://doi.org/10.1021/acsami.6c06092
ACS Appl. Mater. Interfaces 2026, 18, 39941−39951

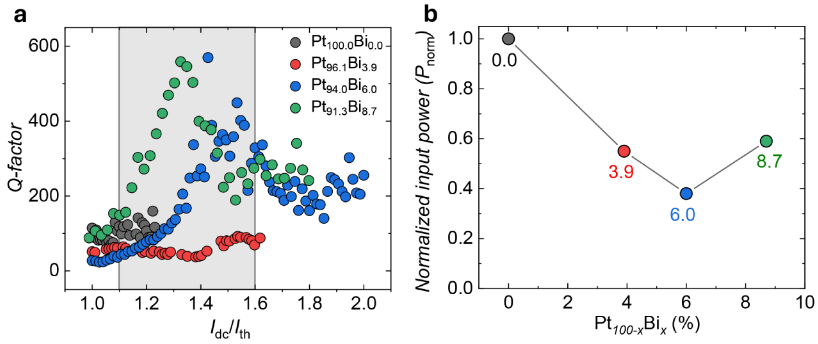

Figure 6. (a) Q factor for 100 nm wide SHNOs with varying Bi content in $Pt_{100-x}Bi_x$ alloys as a function of I_{dc}/I_{th}. The values are normalized with the respective I_{th}. Data are extracted from Figures 4d–g and S9a–d. The shaded gray region indicates the normalized current range I_{dc}/I_{th} = 1.1–1.6 used for comparison. The figure highlights the performance enhancement due to Bi doping, showing the reduction in linewidth and threshold current, as well as the improvement in output power and Q factor, particularly at higher Bi concentrations. (b) Normalized input power for 100 nm wide SHNOs, showing a remarkable 61.6% and 41.0% reduction for 6.0% and 8.7% Bi, respectively.

θ_{SH}/T_{int} *vs* σ_{xx}, with values lying in the bad-metal/dirty-metal regime ($\sigma_{xx} \lesssim 10^4\ \Omega^{-1}\ cm^{-1}$). In this regime, a linear dependence of θ_{SH} on σ_{xx} indicates a dominant intrinsic SHE contribution in Pt, as demonstrated by Casanova et al.[67] However, no clear linear trend is observed, suggesting coexistence of intrinsic and extrinsic side-jump scattering mechanisms[36,55,67] (see Figure S11 and Section S12 of the Supporting Information). Moreover, the increase of θ_{SH} and θ_{SH}/T_{int} with ρ_{xx} supports a dominant role of side-jump scattering and/or disorder-enhanced intrinsic contributions.[39] In metals with strong spin–orbit coupling, the anomalous Hall effect scales with ρ_{xx} either linearly (extrinsic skew scattering) or quadratically (extrinsic side-jump scattering or intrinsic mechanisms).[68] Recent studies have established that SHE shares this scaling behavior.[68] The observed quadratic dependence of θ_{SH} or θ_{SH}/T_{int} on ρ_{xx} hints at the contribution of bulk-extrinsic side-jump scattering and rules out significant interfacial Bi effects on SHE, as confirmed by TEM and consistent with bulk alloy characteristics.

To further confirm the mechanism, the intrinsic SHE contribution was subtracted, revealing $\rho_{imp}^{SH} \propto \rho_{imp}^2$, with and without considering T_{int} (Figure 5e,f), indicative of extrinsic side-jump scattering dominance.[34,35,41,55,62] Here, ρ_{imp}^{SH} denotes the impurity-induced spin Hall resistivity, and ρ_{imp} the resistivity due to impurities. Therefore, increasing Bi concentration in Pt enhances extrinsic side-jump scattering, substantially boosting θ_{SH} and reducing the threshold current I_{th} necessary to drive robust AO, thereby enabling energy-efficient SHNOs.

Performance Enhancement in PtBi Alloy SHNOs

The resistivity ρ_{xx} of $Pt_{100-x}Bi_x$ alloys strongly influences SHNO performance and energy efficiency through current redistribution in the nanoconstriction. Together with a modest increase in the AMR ratio at higher Bi concentrations (6.0% and 8.7%; Figures S3 and S6), this leads to enhanced microwave output power. To benchmark SHNO performance for wireless communication applications, we evaluate the quality factor Q, defined as $Q = f/\Delta f$.[21,22,24] As shown in Figure 6a, SHNOs with higher Bi content exhibit reduced linewidths of ≈25 MHz and increased auto-oscillation frequencies, resulting in high quality factors of $Q \approx 350$–550 within the normalized current range I_{dc}/I_{th} = 1.1–1.6. These values correspond to an approximately 4-fold enhancement compared to 0.0% Bi devices.

The effective power consumption of SHNOs is given by $P = I_{th}^2 R$, where I_{th} is the threshold current and R is the total device resistance.[49] The normalized input power, $P_{norm} = P/P_0$ (with P_0 corresponding to 0.0% Bi ($Pt_{100.0}Bi_{0.0}$)), is shown in Figure 6b as a function of Bi concentration. Bi alloying leads to a pronounced reduction in power consumption, reaching a minimum P_{norm} = 0.38 at 6.0% Bi, corresponding to a 61.6% reduction relative to 0.0% Bi. At higher Bi content (8.7%), P_{norm} slightly increases to 0.59 (41.0% reduction), indicating that optimal energy efficiency is achieved at moderate Bi concentrations. This reduction in power consumption is driven by the lowered I_{th} resulting from enhanced spin–orbit torque in PtBi alloys and is comparable to the maximum reductions reported for W–Ta alloy-based SHNOs, where reduced crystallinity/disorder can coexist with enhanced spintronic functionality and enhanced SOT/SHE.[49] Unlike van der Waals (vdW) heterostructures, where high crystalline quality is often essential for spintronic functionality,[69] moderately reduced crystallinity and alloy disorder in PtBi can be beneficial for enhancing the SHE through extrinsic scattering mechanisms.[36] Overall, these results link Bi-induced crystallographic disorder and enhanced θ_{SH} to reduced I_{th}, increased Q factor, and lower power consumption, underscoring the effectiveness of Bi doping for energy-efficient Pt-based SHNOs.

■ CONCLUSION

In summary, we demonstrate that Bi doping in Pt enhances θ_{SH} by over 3-fold and substantially reduces the threshold current I_{th} in SHNOs, enabling a superior ρ_{xx} trade-off crucial for low-power spintronic applications. The concurrent enhancement of θ_{SH} and reduction in I_{th} underscores the reciprocal relationship between the spin Hall effect and auto-oscillations, as revealed by complementary ST-FMR and AO measurements. Due to a lower Δf and higher auto-oscillation frequency (f) at higher Bi concentrations of 6.0% and 8.7%, we obtain a Q factor of ≈ $350 \le Q \le 550$ attained within the I_{dc}/I_{th} range of 1.1–1.6, which is approximately four times higher than that of 0.0% Bi ($Pt_{100.0}Bi_{0.0}$). Due to a reduction in I_{th}, we report a 61.6% reduction in power consumption underlying the performance enhancement in SHNOs for energy-efficient operation. Furthermore, in-plane angular-dependent ST-FMR confirms a $\sin 2\phi \cos \phi$ symmetry across all $Pt_{100-x}Bi_x$ alloys, indicative

https://doi.org/10.1021/acsami.6c06092
ACS Appl. Mater. Interfaces 2026, 18, 39941–39951

of a bulk-origin, conventional spin−orbit torque mechanism. GIXRD analysis and diffractograms from HR-TEM confirm that increased Bi doping in Pt leads to progressive reduction in crystallinity, significant peak broadening, and preferred crystallographic orientation, indicating structural modifications in the $Pt_{100-x}Bi_x$ alloys. These findings are corroborated by cross-sectional TEM and STEM-EDXS intensity line profiles, which reveal a uniform distribution of Bi throughout the Pt layer and a concurrent loss of Pt crystallinity. The nonlinear dependence of θ_{SH} on σ_{xx} and ρ_{xx} further reveals a $\rho_{imp}^{SH} \propto \rho_{imp}^2$ scaling, with and without the T_{int} factor, confirming extrinsic side-jump scattering as the dominant mechanism behind the enhanced SHE. Collectively, our findings establish a framework for energy-efficient spintronics beyond conventional 5d transition metals. By demonstrating Bi alloying with Pt as an effective strategy for enhancing charge-to-spin conversion, our work offers design principles for next-generation SHNOs for applications in neuromorphic computing, SOT-MRAM, Ising machines, GHz spintronic devices, and wireless communication.

■ EXPERIMENTAL SECTION

Thin Film Preparation

High-resistance silicon (HR-Si) wafers (>10,000 Ω·cm) were used as substrates. The $Pt_{100-x}Bi_x$(4.0 nm)/$Co_{40}Fe_{40}B_{20}$(3.0 nm) stacks were grown on HR-Si/Ta(2.4 nm). Control samples, $Co_{40}Fe_{40}B_{20}$(3.0 nm) and Ta(2.4 nm) were grown on HR-Si. All samples were further protected with a capping layer of MgO(2.0 nm)/SiO_2(3.0 nm). Ta and $Co_{40}Fe_{40}B_{20}$ were sputtered at 11 W with 13.90 ± 0.06 sccm Ar flow at a base pressure of 4×10^{-8} mbar, rising to 4×10^{-3} mbar during deposition. Other layers were deposited via electron beam evaporation. $Pt_{100-x}Bi_x$ was synthesized *in situ* by coevaporation, with deposition rates monitored using a quartz crystal microbalance (QCM). The Bi source was stabilized before Pt adjustment. The deposition rate ratio required to achieve the desired $Pt_{100-x}Bi_x$ composition was calculated as $\frac{v_a}{v_b} = \frac{M_a \rho_b}{M_b \rho_a} \cdot r$, where v_a and v_b are the deposition rates, M_a and M_b are the molar masses, ρ_a and ρ_b are the material densities, and r is the target molar ratio.[51]

Grazing-Incidence X-ray Diffraction (GIXRD)

GIXRD measurements were used to determine the full-width-at-half-maximum (FWHM) of the diffraction peaks. Data were acquired using a Mat:Nordic SAXSLAB instrument with a Rigaku 003 microfocusing Cu X-ray source (parallel beam from a two-bounce monochromator) and two Dectris detectors: Pilatus3 300KR (orthogonal) and 100K (goniometer circle). The beam path was evacuated to suppress air scattering, and a 1° incidence angle was employed to maximize signal intensity. Two-dimensional diffraction images were processed using SAXSGUI. FWHM values and lattice parameters were determined using TOPAS v6 (Bruker AXS, 2016), applying a pure platinum ($Fm\bar{3}m$) structural model and a pseudo-Voigt (PVII) profile. Peak broadening was analyzed separately. Exposure time was 3 h per sample. Instrumental broadening was assessed using LaB_6 powder.

Cross-Sectional TEM Imaging and STEM-EDXS

TEM measurements were carried out using a JEOL monochromatic ARM200F microscope, which is equipped with a Schottky field emission gun, a double-Wien monochromator, a probe aberration corrector, an image aberration corrector, a Gatan image filter (GIF) Continuum, a Gatan OneView camera, as well as a double silicon drift detector (SDD) for energy-dispersive X-ray spectroscopy (EDXS). The microscope was operated at 200 kV for the TEM measurements. TEM specimens were prepared using an FEI Versa 3D focused ion beam-scanning electron microscope (FIB-SEM). After depositing a protective layer containing Pt and C using first the electron beam and then the Ga ion beam in the FIB-SEM, a lamella of the material was cut out using an ion beam at 30 kV and 1 nA. After transferring the lamella to a Cu TEM grid, the lamella was gradually thinned down by the ion beam. The thinning process was performed first at 30 kV with a gradually decreasing beam current from 1 nA to 100 pA. Then, gentle polishing of the specimen was carried out with ion beam energies of 5 kV and 2 kV to minimize ion beam effects.

Device Fabrication

ST-FMR bars ($14 \times 4\ \mu m^2$) and SHNOs with a width of 100 nm were fabricated via electron-beam lithography (Raith EBPG 5200), followed by Ar-ion milling. The GSG-CPW contact pads were subsequently fabricated by mask-less ultraviolet lithography (Heidelberg Instruments MLA 150) and a liftoff technique, followed by Cu(800 nm)/Pt(20 nm) electrodes deposited by DC magnetron sputtering. The detailed fabrication process can be found in ref 70.

AMR, ST-FMR, and AO Measurements

The AMR of all SHNOs and ST-FMR bars was extracted from two-point resistance measurements performed with a rotatable in-plane magnetic field using a Keithley 2182A nanovoltmeter and a Keithley 6221 DC and AC current source. ST-FMR measurements were conducted with a PhaseFMR-40ST instrument from NanOsc Instruments AB. For angular ST-FMR measurements, the sample was measured under a rotatable in-plane magnetic field using a Rohde and Schwarz SMB100A signal generator and a Stanford Research Systems SR830 lock-in amplifier to generate I_{rf} and detect the ST-FMR voltage V_{dc}, respectively. For AO measurements, I_{dc} was applied using a Keithley 2400 sourcemeter, and the AO signal was amplified using a Low Noise Factory (LNF) LNR4 14B low-noise amplifier and detected using a Rohde and Schwarz FSV spectrum analyzer with a resolution bandwidth of 1 MHz. All measurements were performed at room temperature.

Statistical Analysis

The mean deviation (MD) quantifies dispersion in a data set x_1, x_2, ..., x_n and is computed with respect to the mean ($\bar{x}$) or median (M). The mean deviation about the mean is

$$MD_{\bar{x}} = \frac{1}{n} \sum_{i=1}^{n} |x_i - \bar{x}|$$

where $\bar{x}$ is the arithmetic mean, $\bar{x} = \frac{1}{n} \sum_{i=1}^{n} x_i$. Here, $|x_i - \bar{x}|$ represents the absolute deviation from the mean.

■ ASSOCIATED CONTENT

Data Availability Statement

The data that support the findings of this study are available from the corresponding authors upon reasonable request.

SI Supporting Information

The Supporting Information is available free of charge at https://pubs.acs.org/doi/10.1021/acsami.6c06092.

HAADF-STEM and STEM-EDXS characterization; angular-dependent AMR and ST-FMR measurements; power consumption analysis; auto-oscillation measurements at additional external magnetic fields; threshold current extraction; spin Hall nano-oscillator performance analysis; spin mixing conductance and interfacial spin transparency analysis; spin Hall performance comparison of Pt-based alloys; and spin Hall effect mechanism (PDF)

AUTHOR INFORMATION

Corresponding Authors

Markus Münzenberg − *Institut für Physik, Universität Greifswald, Greifswald 17489, Germany;* Email: markus.muenzenberg@uni-greifswald.de

Johan Åkerman − *Applied Spintronics Group, Department of Physics, University of Gothenburg, Gothenburg 412 96, Sweden; Research Institute of Electrical Communication and Center for Science and Innovation in Spintronics, Tohoku University, Sendai 980-8577, Japan;* orcid.org/0000-0002-3513-6608; Email: johan.akerman@physics.gu.se

Authors

Utkarsh Shashank − *Applied Spintronics Group, Department of Physics, University of Gothenburg, Gothenburg 412 96, Sweden;* orcid.org/0000-0001-9032-1841

Akash Kumar − *Applied Spintronics Group, Department of Physics, University of Gothenburg, Gothenburg 412 96, Sweden; Research Institute of Electrical Communication and Center for Science and Innovation in Spintronics, Tohoku University, Sendai 980-8577, Japan;* orcid.org/0000-0002-4105-3681

Tahereh Sadat Parvini − *Institut für Physik, Universität Greifswald, Greifswald 17489, Germany; Walther-Meißner-Institut, Bayerische Akademie der Wissenschaften, Garching 85748, Germany; Munich Center for Quantum Science and Technology (MCQST), Munich 80799, Germany*

Hauke Heyen − *Institut für Physik, Universität Greifswald, Greifswald 17489, Germany;* orcid.org/0000-0002-8577-5002

Lunjie Zeng − *Department of Physics and Astronomy, Chalmers University of Technology, Gothenburg 412 96, Sweden;* orcid.org/0000-0002-4564-7217

Andrew B. Yankovich − *Department of Physics and Astronomy, Chalmers University of Technology, Gothenburg 412 96, Sweden;* orcid.org/0000-0002-1772-6778

Jong-Guk Choi − *Applied Spintronics Group, Department of Physics, University of Gothenburg, Gothenburg 412 96, Sweden;* orcid.org/0000-0002-8915-502X

Mona Rajabali − *NanOsc AB, Kista 164 40, Sweden*

Eva Olsson − *Department of Physics and Astronomy, Chalmers University of Technology, Gothenburg 412 96, Sweden;* orcid.org/0000-0002-3791-9569

Complete contact information is available at: https://pubs.acs.org/10.1021/acsami.6c06092

Author Contributions

U.S., A.K., T.S.P., M.M., and J.Å. initiated the idea and planned the study. H.H. prepared the thin films with input from T.S.P. and A.K.; A.K. fabricated the devices. U.S. performed all electrical auto-oscillation, spin−orbit torque measurements, and analysis with input from A.K., J.-G.C., and M.R.; L.Z. and A.B.Y. performed TEM measurements with input from E.O., J.Å. and M.M. coordinated and supervised the project. All authors contributed to the data analysis and interpretation of the results and cowrote the manuscript.

Notes

The authors declare no competing financial interest.

ACKNOWLEDGMENTS

Financial support from the Horizon 2020 research and innovation programme (Grant Nos. 899559 "SpinAge" and 835068 "TOPSPIN"), the Swedish Research Council (VR Grant No. 2024-01943), and the Marie Skłodowska-Curie grant agreement No. 101152484 "GOHE", is gratefully acknowledged. Financial support from the Swedish Research Council (VR) and the Swedish Foundation for Strategic Research (SSF) for access to ARTEMI, the Swedish National Infrastructure in Advanced Electron Microscopy (Grant Nos. 2021-00171 and RIF21-0026), is also acknowledged. This work was performed in part at the Chalmers Material Analysis Laboratory (CMAL). T.S.P. acknowledges funding from the Deutsche Forschungsgemeinschaft (DFG, German Research Foundation) under Germany's Excellence Strategy − EXC-2111 − 390814868 (MCQST). We thank Dr. Michał Strach (CMAL) for his assistance and insightful discussions regarding the GIXRD measurements.

REFERENCES

(1) Shao, Q.; Li, P.; Liu, L.; Yang, H.; Fukami, S.; Razavi, A.; Wu, H.; Wang, K.; Freimuth, F.; Mokrousov, Y.; Stiles, M. D.; Emori, S.; Hoffmann, A.; Åkerman, J.; Roy, K.; Wang, J.-P.; Yang, S.-H.; Garello, K.; Zhang, W. Roadmap of spin−orbit torques. *IEEE Trans. Magn* **2021**, *57*, 1−39.

(2) Hirsch, J. Spin Hall effect. *Phys. Rev. Lett* **1999**, *83*, 1834.

(3) Dyakonov, M. I.; Perel, V. Current-induced spin orientation of electrons in semiconductors. *Phys. Lett. A* **1971**, *35*, 459.

(4) Dieny, B.; Prejbeanu, I. L.; Garello, K.; Gambardella, P.; Freitas, P.; Lehndorff, R.; Raberg, W.; Ebels, U.; Demokritov, S. O.; Akerman, J.; Deac, A.; Pirro, P.; Adelmann, C.; Anane, A.; Chumak, A. V.; Hirohata, A.; Mangin, S.; Valenzuela, S. O.; Onbasli, M. C.; d'Aquino, G.; Prenat, G.; Finocchio, G.; Lopez-Diaz, L.; Chantrell, R.; Chubykalo-Fesenko, O.; Bortolotti, P. Opportunities and challenges for spintronics in the microelectronics industry. *Nat. Electron* **2020**, *3*, 446−459.

(5) Liu, L.; Pai, C.-F.; Li, Y.; Tseng, H. W.; Ralph, D. C.; Buhrman, R. A. Spin-Torque Switching with the Giant Spin Hall Effect of Tantalum. *Science* **2012**, *336*, 555.

(6) Yu, G.; Upadhyaya, P.; Fan, Y.; Alzate, J. G.; Jiang, W.; Wong, K. L.; Takei, S.; Bender, S. A.; Chang, L.-T.; Jiang, Y.; Lang, M.; Tang, J.; Wang, Y.; Tserkovnyak, Y.; Amiri, P. K.; Wang, K. L. Switching of perpendicular magnetization by spin−orbit torques in the absence of external magnetic fields. *Nat. Nanotechnol* **2014**, *9*, 548−554.

(7) Miron, I. M.; Garello, K.; Gaudin, G.; Zermatten, P.-J.; Costache, M. V.; Auffret, S.; Bandiera, S.; Rodmacq, B.; Schuhl, A.; Gambardella, P. Perpendicular switching of a single ferromagnetic layer induced by in-plane current injection. *Nature* **2011**, *476*, 189−193.

(8) Cai, K.; Talmelli, G.; Fan, K.; Van Beek, S.; Kateel, V.; Gupta, M.; Monteiro, M. G. J.; Ben Chroud, M.; Jayakumar, G.; Trovato, A., et al. *2022 International Electron Devices Meeting (IEDM)*. IEEE 2022; pp 36.2.1−36.2.4.

(9) Fulara, H.; Zahedinejad, M.; Khymyn, R.; Awad, A. A.; Muralidhar, S.; Dvornik, M.; Åkerman, J. Spin-orbit torque−driven propagating spin waves. *Sci. Adv* **2019**, *5*, No. eaax8467.

(10) Kumar, A.; Chaurasiya, A. K.; González, V. H.; Behera, N.; Alemán, A.; Khymyn, R.; Awad, A. A.; Åkerman, J. Spin-wave-mediated mutual synchronization and phase tuning in spin Hall nano-oscillators. *Nat. Phys* **2025**, *21*, 245.

(11) Demidov, V. E.; Urazhdin, S.; Zholud, A.; Sadovnikov, A. V.; Demokritov, S. O. Nanoconstriction-based spin-Hall nano-oscillator. *Appl. Phys. Lett* **2014**, *105*, 172410.

(12) Kumar, A.; Litvinenko, A.; Behera, N.; Awad, A. A.; Khymyn, R.; Åkerman, J.Mutual synchronization in spin-torque and spin Hall nano-oscillators*Nanomagnets as Dynamical Systems: Physics and Applications*; Springer, 2024, pp 143.

(13) Emori, S.; Bauer, U.; Ahn, S.-M.; Martinez, E.; Beach, G. S. Current-driven dynamics of chiral ferromagnetic domain walls. *Nat. Mater* **2013**, *12*, 611.
(14) Bernstein, N.; Li, H.; Assouline, B.; Lau, Y.-C.; Rozhansky, I.; Wang, W.; Capua, A. Spin-torque skyrmion resonance in a frustrated magnet. *Nat. Commun* **2025**, *16*, 4616.
(15) Khvalkovskiy, A.; Cros, V.; Apalkov, D.; Nikitin, V.; Krounbi, M.; Zvezdin, K.; Anane, A.; Grollier, J.; Fert, A. Matching domain-wall configuration and spin-orbit torques for efficient domain-wall motion. *Phys. Rev. B* **2013**, *87*, 020402.
(16) Liu, L.; Moriyama, T.; Ralph, D.; Buhrman, R. Spin-torque ferromagnetic resonance induced by the spin Hall effect. *Phys. Rev. Lett* **2011**, *106*, 036601.
(17) Liu, R.; Lim, W.; Urazhdin, S. Spectral characteristics of the microwave emission by the spin Hall nano-oscillator. *Phys. Rev. Lett* **2013**, *110*, 147601.
(18) Kasai, S.; Kondou, K.; Sukegawa, H.; Mitani, S.; Tsukagoshi, K.; Otani, Y. Modulation of effective damping constant using spin Hall effect. *Appl. Phys. Lett* **2014**, *104*, 092408.
(19) Chen, T.; Dumas, R. K.; Eklund, A.; Muduli, P. K.; Houshang, A.; Awad, A. A.; Dürrenfeld, P.; Malm, B. G.; Rusu, A.; Åkerman, J. Spin-torque and spin-Hall nano-oscillators. *Proc. IEEE* **2016**, *104*, 1919.
(20) Awad, A.; Dürrenfeld, P.; Houshang, A.; Dvornik, M.; Iacocca, E.; Dumas, R.; Åkerman, J. Long-range mutual synchronization of spin Hall nano-oscillators. *Nat. Phys* **2017**, *13*, 292.
(21) Kumar, A.; Fulara, H.; Khymyn, R.; Litvinenko, A.; Zahedinejad, M.; Rajabali, M.; Zhao, X.; Behera, N.; Houshang, A.; Awad, A. A.; et al. Robust mutual synchronization in long spin Hall nano-oscillator chains. *Nano Lett* **2023**, *23*, 6720.
(22) Zahedinejad, M.; Awad, A. A.; Muralidhar, S.; Khymyn, R.; Fulara, H.; Mazraati, H.; Dvornik, M.; Åkerman, J. Two-dimensional mutually synchronized spin Hall nano-oscillator arrays for neuromorphic computing. *Nat. Nanotechnol* **2020**, *15*, 47.
(23) Behera, N.; Chaurasiya, A. K.; González, V. H.; Litvinenko, A.; Bainsla, L.; Kumar, A.; Khymyn, R.; Awad, A. A.; Fulara, H.; Åkerman, J. Ultra-Low Current 10 nm Spin Hall Nano-Oscillators. *Adv. Mater* **2024**, *36*, 2305002.
(24) Behera, N.; Chaurasiya, A. K.; Kumar, A.; Khymyn, R.; Litvinenko, A.; Bainsla, L.; Awad, A. A.; Åkerman, J. Ultra-large mutually synchronized networks of 10 nm spin Hall nano-oscillators. *arXiv*. **2025**.
(25) Zahedinejad, M.; Fulara, H.; Khymyn, R.; Houshang, A.; Dvornik, M.; Fukami, S.; Kanai, S.; Ohno, H.; Åkerman, J. Memristive control of mutual spin Hall nano-oscillator synchronization for neuromorphic computing. *Nat. Mater* **2022**, *21*, 81.
(26) Torrejon, J.; Riou, M.; Araujo, F. A.; Tsunegi, S.; Khalsa, G.; Querlioz, D.; Bortolotti, P.; Cros, V.; Yakushiji, K.; Fukushima, A.; Kubota, H.; Yuasa, S.; Stiles, M. D.; Grollier, J. Neuromorphic computing with nanoscale spintronic oscillators. *Nature* **2017**, *547*, 428−431.
(27) Grollier, J.; Querlioz, D.; Camsari, K.; Everschor-Sitte, K.; Fukami, S.; Stiles, M. D. Neuromorphic spintronics. *Nat. Electron* **2020**, *3*, 360.
(28) Houshang, A.; Zahedinejad, M.; Muralidhar, S.; Chęciński, J.; Khymyn, R.; Rajabali, M.; Fulara, H.; Awad, A. A.; Dvornik, M.; Åkerman, J. Phase-binarized spin Hall nano-oscillator arrays: Towards spin Hall ising machines. *Phys. Rev. Appl* **2022**, *17*, 014003.
(29) Choi, J.-G.; Park, J.; Kang, M.-G.; Kim, D.; Rieh, J.-S.; Lee, K.-J.; Kim, K.-J.; Park, B.-G. Voltage-driven gigahertz frequency tuning of spin Hall nano-oscillators. *Nat. Commun* **2022**, *13*, 3783.
(30) Wang, Y.; Deorani, P.; Qiu, X.; Kwon, J. H.; Yang, H. Determination of intrinsic spin Hall angle in Pt. *Appl. Phys. Lett* **2014**, *105*, 152412.
(31) Nguyen, M.-H.; Ralph, D.; Buhrman, R. Spin torque study of the spin Hall conductivity and spin diffusion length in platinum thin films with varying resistivity. *Phys. Rev. Lett* **2016**, *116*, 126601.
(32) Zhang, W.; Han, W.; Jiang, X.; Yang, S.-H.; Parkin, S. S. P. Role of transparency of platinum−ferromagnet interfaces in determining the intrinsic magnitude of the spin Hall effect. *Nat. Phys* **2015**, *11*, 496−502.
(33) Shashank, U.; Medwal, R.; Shibata, T.; Nongjai, R.; Vas, J. V.; Duchamp, M.; Asokan, K.; Rawat, R. S.; Asada, H.; Gupta, S.; et al. Enhanced Spin Hall effect in S-implanted Pt. *Adv. Quantum Technol* **2021**, *4*, 2000112.
(34) Shashank, U.; Medwal, R.; Nakamura, Y.; Mohan, J. R.; Nongjai, R.; Kandasami, A.; Rawat, R. S.; Asada, H.; Gupta, S.; Fukuma, Y. Highly dose dependent damping-like spin−orbit torque efficiency in O-implanted Pt. *Appl. Phys. Lett* **2021**, *118*, 252406.
(35) Shashank, U.; Nakamura, Y.; Kusaba, Y.; Tomoda, T.; Nongjai, R.; Kandasami, A.; Medwal, R.; Rawat, R. S.; Asada, H.; Gupta, S.; Fukuma, Y. Disentanglement of intrinsic and extrinsic side-jump scattering induced spin Hall effect in N-implanted Pt. *Phys. Rev. B* **2023**, *107*, 064402.
(36) Shashank, U.; Tomoda, T.; Mathew, A. J.; Vashisht, G.; Imai, K.; Kusaba, Y.; Dong, C.-L.; Chen, C.-L.; Horibe, Y.; Ishimaru, M.; et al. Giant spin-orbit torque induced by spin Hall effect in amorphous Pt (P) alloys. *NPG Asia Mater* **2025**, *17*, 15.
(37) Yang, L.; Fei, Y.; Zhou, K.; Chen, L.; Fu, Q.; Li, L.; Yan, C.; Li, H.; Du, Y.; Liu, R. Maximizing spin−orbit torque efficiency of Ta(O)/Py via modulating oxygen-induced interface orbital hybridization. *Appl. Phys. Lett* **2021**, *118*, 032405.
(38) Demasius, K.-U.; Phung, T.; Zhang, W.; Hughes, B. P.; Yang, S.-H.; Kellock, A.; Han, W.; Pushp, A.; Parkin, S. S. P. Enhanced spin−orbit torques by oxygen incorporation in tungsten films. *Nat. Commun* **2016**, *7*, 10644.
(39) Chen, T.-Y.; Wu, C.-T.; Yen, H.-W.; Pai, C.-F. Tunable spin-orbit torque in Cu-Ta binary alloy heterostructures. *Phys. Rev. B* **2017**, *96*, 104434.
(40) Wang, P.; Migliorini, A.; Yang, S.-H.; Jeon, J.-C.; Kostanovskiy, I.; Meyerheim, H.; Han, H.; Deniz, H.; Parkin, S. S. P. Giant spin Hall effect and spin−orbit torques in 5d transition metal−aluminum alloys from extrinsic scattering. *Adv. Mater* **2022**, *34*, No. e2109406.
(41) Ramaswamy, R.; Wang, Y.; Elyasi, M.; Motapothula, M.; Venkatesan, T.; Qiu, X.; Yang, H. Extrinsic spin Hall effect in $Cu_{1-x}Pt_x$. *Phys. Rev. Appl* **2017**, *8*, 024034.
(42) Zhu, L.; Sobotkiewich, K.; Ma, X.; Li, X.; Ralph, D. C.; Buhrman, R. A. Strong damping-like spin−orbit torque and tunable Dzyaloshinskii−Moriya interaction generated by low-resistivity $Pd_{1-x}Pt_x$ alloys. *Adv. Funct. Mater* **2019**, *29*, 1805822.
(43) Ma, L.; Zhou, H.-A.; Wang, L.; Fan, X.-L.; Fan, W.-J.; Xue, D.-S.; Xia, K.; Wang, Z.; Wu, R.-Q.; Guo, G.-Y.; et al. Spin Orbit Coupling Controlled Spin Pumping and Spin Hall Magnetoresistance Effects. *Adv. Electron. Mater* **2016**, *2*, 1600112.
(44) Hong, C.; Jin, L.; Zhang, H.; Li, M.; Rao, Y.; Ma, B.; Li, J.; Zhong, Z.; Yang, Q. Giant inverse spin Hall effect in Bi doped PtBi alloy. *Adv. Electron. Mater* **2018**, *4*, 1700632.
(45) Bekele, Z. A.; Li, R.; Li, Y.; Cao, Y.; Liu, X.; Wang, K. Tuning the High-Efficiency Field-Free Current-Induced Deterministic Switching via Ultrathin PtMo Layer with Mo Content. *Adv. Electron. Mater* **2021**, *7*, 2100528.
(46) Bekele, Z. A.; Liu, X.; Cao, Y.; Wang, K. High-Efficiency Spin−Orbit Torque Switching Using a Single Heavy-Metal Alloy with Opposite Spin Hall Angles. *Adv. Electron. Mater* **2021**, *7*, 2000793.
(47) Zhu, L.; Ralph, D. C.; Buhrman, R. A. Highly efficient spin-current generation by the spin Hall effect in $Au_{1-x}Pt_x$. *Phys. Rev. Appl* **2018**, *10*, 031001.
(48) Obstbaum, M.; Decker, M.; Greitner, A.; Haertinger, M.; Meier, T. N. G.; Kronseder, M.; Chadova, K.; Wimmer, S.; Ködderitzsch, D.; Ebert, H.; et al. Tuning spin Hall angles by alloying. *Phys. Rev. Lett* **2016**, *117*, 167204.
(49) Behera, N.; Fulara, H.; Bainsla, L.; Kumar, A.; Zahedinejad, M.; Houshang, A.; Åkerman, J. Energy-Efficient $W_{100-x}Ta_x$/Co-Fe-B/MgO Spin Hall Nano-Oscillators. *Phys. Rev. Appl* **2022**, *18*, 024017.
(50) Chi, Z.; Lau, Y.-C.; Kawaguchi, M.; Hayashi, M. Charge−spin conversion in $Pt_{1-x}Bi_x$ alloys for spin−orbit torque switching. *APL Mater* **2021**, *9*, 061111.

(51) Winkel, T. J.; Parvini, T. S.; Stiewe, F.-F.; Walowski, J.; Moradi, F.; Münzenberg, M. Comparative analysis of THz signal emission from bilayer heterostructures: Wideband and high-frequency THz signal advantage of PtBi-based emitter. *Appl. Phys. Lett* **2024**, *124*, 012408.

(52) Feng, Y.; Jiang, Q.; Feng, B.; Yang, M.; Xu, T.; Liu, W.; Yang, X.; Arita, M.; Schwier, E. F.; Shimada, K.; et al. Rashba-like spin splitting along three momentum directions in trigonal layered PtBi2. *Nat. Commun* **2019**, *10*, 4765.

(53) Schimmel, S.; Fasano, Y.; Hoffmann, S.; Besproswanny, J.; Corredor Bohorquez, L. T.; Puig, J.; Elshalem, B.-C.; Kalisky, B.; Shipunov, G.; Baumann, D.; et al. Surface superconductivity in the topological Weyl semimetal t-PtBi2. *Nat. Commun* **2024**, *15*, 9895.

(54) Lau, Y.-C.; Seki, T.; Takanashi, K. Highly fcc-textured Pt−Al alloy films grown on MgO (001) showing enhanced spin Hall efficiency. *APL Mater* **2021**, *9*, 081113.

(55) Shashank, U.; Kusaba, Y.; Nakamura, J.; Mathew, A. J.; Imai, K.; Senba, S.; Asada, H.; Fukuma, Y. Charge−spin interconversion in nitrogen sputtered Pt via extrinsic spin Hall effect. *J. Phys.: Condens. Matter* **2024**, *36*, 325802.

(56) Nan, T.; Emori, S.; Boone, C. T.; Wang, X.; Oxholm, T. M.; Jones, J. G.; Howe, B. M.; Brown, G. J.; Sun, N. X. Comparison of spin-orbit torques and spin pumping across NiFe/Pt and NiFe/Cu/Pt interfaces. *Phys. Rev. B* **2015**, *91*, 214416.

(57) Harder, M.; Gui, Y.; Hu, C.-M. Electrical detection of magnetization dynamics via spin rectification effects. *Phys. Rep* **2016**, *661*, 1.

(58) Mohan, J. R.; Shashank, U.; Deka, A.; Hanashima, T.; Medwal, R.; Gupta, S.; Rawat, R. S.; Asada, H.; Fukuma, Y. Observation of Out-of-Plane Antidamping Torque at the Platinum/Permalloy Interface. *ACS Appl. Mater. Interfaces* **2025**, *17*, 11259.

(59) Gupta, P.; Khan, K. I. A.; Kumar, A.; Sahu, P.; Agarwal, R.; Litvinenko, A.; Kandwal, N.; Yadav, R. S.; Nanda, B. R. K.; Åkerman, J.; et al. Symmetry enhanced unconventional spin current anisotropy in a collinear antiferromagnet. *Adv. Funct. Mater* **2026**, *36*, No. e06816.

(60) Kumar, A.; Shashank, U.; Maharana, S. K.; Mohan, J. R.; Vas, J. V.; Gupta, S.; Asada, H.; Dunin-Borkowski, R. E.; Fukuma, Y.; Medwal, R. Charge-to-spin conversion at argon ion milled SrTiO3/NiFe hetero-interfaces. *Appl. Phys. Lett* **2025**, *126*, 032401.

(61) Bainsla, L.; Kumar, A.; Awad, A. A.; Wang, C.; Zahedinejad, M.; Behera, N.; Fulara, H.; Khymyn, R.; Houshang, A.; Weissenrieder, J.; et al. Ultrathin ferrimagnetic GdFeCo films with low damping. *Adv. Funct. Mater* **2022**, *32*, 2111693.

(62) Kumar, A.; Bansal, R.; Chaudhary, S.; Muduli, P. K. Large spin current generation by the spin Hall effect in mixed crystalline phase Ta thin films. *Phys. Rev. B* **2018**, *98*, 104403.

(63) Wang, Y.; Ramaswamy, R.; Yang, H. FMR-related phenomena in spintronic devices. *J. Phys. D: Appl. Phys* **2018**, *51*, 273002.

(64) Kittel, C. On the Theory of Ferromagnetic Resonance Absorption. *Phys. Rev* **1948**, *73*, 155.

(65) Dvornik, M.; Awad, A. A.; Åkerman, J. Origin of magnetization auto-oscillations in constriction-based spin Hall nano-oscillators. *Phys. Rev. Appl* **2018**, *9*, 014017.

(66) Arunima, T. M.; Fulara, H. Tunable current−field minima induced by demagnetizing fields in nano-constriction spin Hall nano-oscillators. *Appl. Phys. Lett* **2025**, *127*, 092403.

(67) Sagasta, E.; Omori, Y.; Isasa, M.; Gradhand, M.; Hueso, L. E.; Niimi, Y.; Otani, Y.; Casanova, F. Tuning the spin Hall effect of Pt from the moderately dirty to the superclean regime. *Phys. Rev. B* **2016**, *94*, 060412.

(68) Sinova, J.; Valenzuela, S. O.; Wunderlich, J.; Back, C. H.; Jungwirth, T. Spin Hall effects. *Rev. Mod. Phys* **2015**, *87*, 1213.

(69) Shinwari, T.; Khan, K. I. A.; Lv, H.; Kassa, A. A.; Munnik, F.; Josephy, S.; Trampert, A.; Ukleev, V.; Luo, C.; Radu, F.; Herfort, J.; Hanke, M.; Lopes, J. M. J. Above-Room-Temperature Ferromagnetism in Large-Scale Epitaxial Fe3GaTe2/Graphene van der Waals Heterostructures. *ACS Nano* **2025**, *19*, 37561−37571.

(70) Kumar, A.; Rajabali, M.; González, V. H.; Zahedinejad, M.; Houshang, A.; Åkerman, J. Fabrication of voltage-gated spin Hall nano-oscillators. *Nanoscale* **2022**, *14*, 1432.

https://doi.org/10.1021/acsami.6c06092
ACS Appl. Mater. Interfaces 2026, 18, 39941−39951